Control of Metal–Organic Framework Crystallization by Metastable Intermediate Pre-equilibrium Species†

Hamish H-M Yeung,*[a] Adam F Sapnik,[a] Felicity Massingberd-Mundy,[a] Michael W Gaultois,[b] Yue Wu,[c] Duncan A X Fraser,[a] Sebastian Henke,[d] Roman Pallach,[d] Niclas Heidenreich,[e,f] Oxana Magdysyuk,[g] Nghia T Vo,[g] and Andrew L Goodwin.[a]

[a] *Inorganic Chemistry Laboratory, University of Oxford, South Parks Road, Oxford, UK.*

[b] *Leverhulme Research Center for Functional Material Design, The Materials Innovation Factory, Department of Chemistry, University of Liverpool, UK.*

[c] *Department of Materials Science & Engineering, National University of Singapore, Singapore.*

[d] *Technische Universität Dortmund, Anorganische Chemie, Otto-Hahn-Str. 6, Dortmund, Germany*

[e] *Institut für Anorganischen Chemie, Christian-Albrechts-Universität zu Kiel, Germany.*

[f] *Deutsches-Elektronen-Synchrotron DESY, Germany.*

[g] *Beamline I12 - JEEP, Diamond Light Source Ltd., Harwell Campus, Didcot, UK.*

**Tel: +44 1865 272610; E-mail: hamish.yeung@chem.ox.ac.uk*

Metal–organic frameworks (MOFs) show exceptional promise for gas separation,[1] sensing,[2] catalysis,[3] and other applications, owing to their modular, porous architecture based on metal nodes and organic linkers.[4,5] The processes of MOF nucleation and crystal growth are fundamentally important to particle size and shape,[6] yield and efficiency in industrial scale-up,[7] and phase selection.[8] Yet, despite increasing awareness, the crystallization of MOFs is poorly understood.[9,10] ZIF-8, $[Zn(mIm)_2]$ (mImH = 2-methylimidazole) shows potential for carbon capture, propene/propane separations and dielectric applications[11] and is one of the few MOFs that have been investigated in detail as a model system for MOF crystallization.[12–19] ZIF-8 nanoparticles were first synthesised by Cravillon *et al.* in 2009, using excess mImH to deprotonate linkers and terminate particle surfaces.[12] Static light scattering revealed slow, continuous nucleation and fast crystal growth;[14] *in situ* X-ray diffraction (XRD) suggested that the crystallization process is phase-boundary-limited,[20,21] as evidenced by the Avrami exponent, n,[22–24] taking values of $n \approx 1$.[25] However, other XRD measurements reported values ranging from $n = 0.6$ (diffusion-limited) in methanol:aqueous ammonia,[26] to $n = 1$ in heated DMF[27] and $n = 4$ (classical, 3-D monomer attachment) in pure methanol.[28] Small-angle X-ray scattering (SAXS) showed that clusters approximately 1 nm in diameter coalesce to form intermediate amorphous particles,[15] and electrospray ionisation mass spectrometry (ESI-MS) indicated that several different clusters co-exist in the reaction solution.[16] However, *in situ* atomic force microscopy (AFM) revealed that the key species at the crystal surface are individual mImH linkers and solvated Zn^{2+} ions.[17] On the other hand, a recent total scattering investigation suggested that the solution state is dominated by $[Zn(mImH)_4]$–like species.[19] The apparent disparity between these observations indicates that we are far from understanding the chemistry of MOF nucleation and growth, even in such an ostensibly simple system as ZIF-8.

We report a tandem *in situ* XRD and *p*H investigation into ZIF-8 crystallization, in which we show that, under certain conditions, the rate ZIF-8 crystallization decreases with increasing reactant concentration. In order to explain this counterintuitive observation, we propose a model for ZIF-8 crystallization that involves a pre-equilibrium of metastable intermediate clusters with various Zn:mIm ratios and different degrees of protonation. The rate of crystallization depends on the position of equilibrium: owing to favourable Zn–mIm coordination, crystallization from over-stoichiometric clusters is dissociative and slower than crystallization from under-stoichiometric clusters. By considering how the pre-equilibrium is perturbed by changes in concentration, we can rationalise the apparent contradictions between previous observations and identify new ways for controlling crystal size and structure in ZIF-8.

In situ XRD[29–33] data were collected at Beamline I12, Diamond synchrotron,[34] on a series of room temperature reactions in methanol, in which the mImH:Zn ratio was kept constant at 4:1 and the Zn^{2+} concentration, $[Zn^{2+}]_0$, was varied from 0.02 M to 0.10 M in 0.02 M steps. Under these conditions, the crystallization rate was observed to decrease with increasing concentration (Fig. 1a, b). Integrated XRD peak intensities were extracted by Pawley refinements (see Sections S1 and S2 in the Supporting Information) and their changes were fitted to the expression of Gualtieri[35] to give the rates of nucleation, k_N, from $5.57(7) \times 10^{-3} s^{-1}$ to $7.9(4) \times 10^{-4} s^{-1}$ ($[Zn^{2+}]_0 = 0.02$ M to 0.10 M) and growth, k_G, from $2.1(4) \times 10^{-3} s^{-1}$ to $2.67(9) \times 10^{-4} s^{-1}$, confirming that both nucleation and crystal growth are inhibited as concentration increases (Fig. 1c). The single exponent, n, given by the Gualtieri expression[35] ranges from $0.47(4)$ to $1.03(6)$, without an obvious trend with

† Electronic Supplementary Information (ESI) available: detailed experimental methods, *in situ* XRD data, Pawley refinement results, Gualtieri and Sharp-Hancock plots, *in situ p*H and turbidity profile fits, rate constants, and SEM images.

concentration. However, analysis by the Sharp-Hancock method[21] shows that n changes with time, from $n \approx 1$ in the initial stages to $n < 1$ in the later stages, suggesting a progression from phase boundary conditions to diffusion-limited crystallization (see Fig. S28).

A decrease in crystallization rate with increasing concentration cannot be understood by a linear mechanism of MOF crystallization according to the stoichiometric equation, $Zn^{2+} + 2\,mImH \longrightarrow [Zn(mIm)_2] + 2\,H^+$. We propose that crystallization is instead preceded by a pre-equilibrium of metastable intermediate coordination clusters with compositions $[Zn(mIm)_x(mImH)_y(S)_z]^{(2-x)+}$, where S = coordinating solvent (Fig. 2). Although purely solvated Zn^{2+} is six-coordinate, tetrahedral geometries are preferred for linker-coordinated clusters, *i.e.* $x + y + z = 4$.[36] Each cluster exists in dynamic equilibrium with a counterpart of higher mImH:Zn ratio *via* solvent-linker exchange, with equilibrium constant K_c and rate constants k_c and k_{-c} for the forward and reverse reactions, respectively (Eq. 1). A second set of equililbria exists between each species and its deprotonated counterpart, with equilibrium constant K_d and rate constants k_d and k_{-d} (Eq. 2). For simplicity, we assume that all coordination equilibria have the same constants, deprotonation likewise, S is in large excess ([S]:[Zn] $\gg 200$) and mImH ($pK_b = 7.75$ in water)[37] is the only significant base involved. We estimate equilibrium constants to be $K_c \approx 330$ and $K_d \approx 2.8 \times 10^{-3}$ (see Section S1.5). Following pre-equilibrium, the coordination clusters condense to give the stoichiometric crystalline product, $[Zn(mIm)_2]$. Although condensation might in principle occur between any neutral monomer with a deprotonated mIm ligand (*i.e.* $x \geq 1$) and one with a site not coordinated by mIm ($z \geq 1$), in order to define a minimally-parameterized model that qualitatively captures the experimental trends, we use only the simplest neutral monomer species with the best condensation statistics ($x = z = 2$), $[Zn(mIm)_2(S)_2]$. Condensation is described by self-nucleation (Eq. 3) and autocatalytic growth (Eq. 4),with rate constants k_1, and k_2, respectively.[38] We find good qualitative agreement with experiments using values of $k_1 = 100\ s^{-1}$, $k_2 = 10^6\ s^{-1}$, $k_c = 330\ M^{-1}\ s^{-1}$ ($k_{-c} = 1\ M^{-1}\ s^{-1}$) and $k_d = 2800\ M^{-1}\ s^{-1}$ ($k_{-d} = 10^6\ M^{-1}\ s^{-1}$).

$$[Zn(mIm)_x(mImH)_y(S)_z]^{(2-x)+} + mImH \underset{k_{-c}}{\overset{k_c}{\rightleftharpoons}} [Zn(mIm)_x(mImH)_{y+1}(S)_{z-1}]^{(2-x)+} + S, \quad K_c = \frac{k_c}{k_{-c}} \tag{1}$$

$$[Zn(mIm)_x(mImH)_y(S)_z]^{(2-x)+} + mImH \underset{k_{-d}}{\overset{k_d}{\rightleftharpoons}} [Zn(mIm)_{x+1}(mImH)_{y-1}(S)_z]^{(1-x)+} + mImH_2{}^+, \quad K_d = \frac{k_d}{k_{-d}} \tag{2}$$

$$[Zn(mIm)_2(S)_2] \xrightarrow{k_1} [Zn(mIm)_2] + 2\,S \tag{3}$$

$$[Zn(mIm)_2(S)_2] + [Zn(mIm)_2] \xrightarrow{k_2} 2\,[Zn(mIm)_2] + 2\,S \tag{4}$$

The important consequence of this model is that the crystallization rate and mechanism do not depend directly on the concentration of reagents but on the position of pre-equilibrium: when under-stoichiometric species ($x + y < 2$) dominate, crystallization is associative and fast, whereas when over-stoichiometric species dominate, crystallization is limited by the rate of mImH dissociation and is therefore slower. Simulations in COPASI[39] show that before pre-equilibrium is attained, under-coordinated species prevail (Fig. 3a), resulting in associative, nucleation-dominated crystallization (Fig. 3b). However, once pre-equilibrium is reached, clusters become over-coordinated, resulting in a reduction in nucleation relative to growth. At higher concentration, nucleation is initially faster (Fig. 3d) but pre-equilibrium is achieved faster and is pushed further towards over-coordinated species (Fig. 3c), leading to a stronger suppression of crystallization overall (Fig. 3e). Sharp-Hancock analysis suggests that changes in n occur upon changes in the crystallization route (*i.e.* nucleation vs. growth), relative concentrations of intermediates and pH (see Fig. S29).

We test our model by monitoring pH, which allows us to estimate the concentrations of protonated and neutral mImH species (see Sections S1.4 and S1.5 for details). Linear crystallization would give continuous release of $mImH_2{}^+$ and an exponential decay in pH. However, we see a stepwise pH profile in the experimental and simulated data (Fig 4). A rapid decrease from pH 9–10 to 6–7 occurs upon mixing within the time resolution of our experiment (10 s). In the pre-equilibrium model this corresponds to a decrease in the concentration of neutral mImH species ($pK_a = 14.2$ in water)[40] owing to rapid formation of $Zn(mImH)_y$ coordination complexes ($pK_a = 10.3$ in water),[41] and condensation of a few oligomers, which releases $mImH_2{}^+$. As pre-equilibrium is established, the rate of condensation decreases, leading to a plateau in pH. Then autocatalytic crystal growth accelerates and is accompanied by the release of further $mImH_2{}^+$. The resulting second decrease in pH exhibits the same timescale as crystal growth observed by *in situ* XRD (see Fig. S33), which suggests that condensation and crystallization processes are linked. If the rate of crystal growth is related to diffusion of $mImH_2{}^+$, this would be consistent with a value of $n < 1$ found towards the end of the reactions. Evidence that the pre-equilibrium exists in solution, rather than in amorphous particles, comes from *in situ* measurements of turbidity, which display timescale and concentration dependence similar to nucleation, as measured by XRD (see Fig. S33), *i.e.* condensation to form particles occurs during the second pH decrease and not before. *Ex situ* SEM shows that particle diameter increases with increasing concentration (Fig. 5), somewhat in contrast to the expectation of classical, linear crystallization. The pre-equilibrium model explains why this is the case: with increasing concentration, the number of nuclei produced remains constant but, by virtue of increased reactant availability, the average particle size increases (Fig. 5, inset).

Although the simplicity of the condensation process in our model precludes direct fitting to what are undoubtedly very complex crystallization curves, which arise from e.g. surface area and diffusion effects, we emphasise here that the trends in our data are qualitatively well captured. The pre-equilibrium model also helps to rationalise the diversity of previous observations. Highly basic solutions, e.g. a large excess of mImH or NH_3,[12,14–16,26] promote deprotonation and a fast, associative route. Low values of n reflect the diffusion-limit of such rapid crystallization. Increasing concentration favours over-coordinated species; the model correctly predicts the dominance of $[Zn(mImH)_4]$-like species

in such crystallizations.[19] The use of water in the same study also slows crystallization, *via faster* coordination, which allows pre-equilibrium conditions to be more rapidly reached: solvent:ligand exchange at labile ions, such as Zn^{2+}, is limited by solvent dissociation; water exchange is at least an order of magnitude faster than methanol.[42] Finally, in extremely dilute, mildly acidic conditions, the pre-equilibrium favours low coordination numbers and even isolated mImH and $[Zn(S)_z]^{2+}$ species (see Fig. 3a at extended times), resulting in extremely slow crystallization and phase-boundary conditions.[17]

The qualitative importance of *p*H in the thermodynamics and kinetics of MOF formation is already widely known.[43] For example, the synthesis of many MOFs requires decomposition of DMF to release dimethylamine, which acts as a *p*H modifier to induce nucleation. On the other hand, absolute concentration has rarely been used as a synthetic handle to control MOF formation. These results show that, somewhat counterintuitively, increasing concentration can inhibit nucleation by promoting over-coordination, and lead to changes in the growth mechanism. Whilst further verification of the pre-equilibrium model could be demonstrated by performing *in situ* ESI-MS, SAXS or TEM, our results provide a new framework in which to interpret MOF syntheses, predict the effects of tuning different reaction parameters, and relate them to the solution chemistry of the metal and linkers. For instance, *p*H control at high concentrations represents an obvious means to inhibit nucleation of metastable precursor solutions, prior to seeding or addition of base, in order to control particle size or film thickness. In addition, by diversifying the composition of pre-equilibrium species, e.g. *via* dynamic combinatorial chemistry, we may be able to access new phases with specific compositions, local structures, or correlated disorder.

Acknowledgements. The research leading to this result has been supported by Diamond Light Source (beamtime EE16354 & EE16450), the project CALIPSOplus under the Grant Agreement 730872 from the EU Framework Programme for Research and Innovation HORIZON 2020, the SCG Innovation Fund and the Samuel and Violette Glasstone Bequest (HHMY), and the Leverhulme Trust for funding *via* the Leverhulme Research Centre for Functional Materials Design (MWG). We thank Jennifer Holter for assistance with SEM and Richard Cooper for use of the turbidity cell.

References

1 Z. Bao, G. Chang, H. Xing, R. Krishna, Q. Ren, B. Chen, *Energy and Environmental Science* **2016**, *9*, 3612–3641.
2 I. Stassen, N. Burtch, A. Talin, P. Falcaro, M. Allendorf, R. Ameloot, *Chemical Society Reviews* **2017**, *46*, 3185–3241.
3 J. Liu, L. Chen, H. Cui, J. Zhang, L. Zhang, C. Y. Su, *Chemical Society Reviews* **2014**, *43*, 6011–6061.
4 H. Furukawa, K. E. Cordova, M. O'Keeffe, O. M. Yaghi, *Science* **2013**, *341*.
5 V. Guillerm, D. Kim, J. F. Eubank, R. Luebke, X. Liu, K. Adil, M. S. Lah, M. Eddaoudi, *Chemical Society Reviews* **2014**, *43*, 6141–6172.
6 B. Seoane, S. Castellanos, A. Dikhtiarenko, F. Kapteijn, J. Gascon, *Coordination Chemistry Reviews* **2016**, *307*, 147–187.
7 U. Mueller, M. Schubert, F. Teich, H. Puetter, K. Schierle-Arndt, J. Pastré, *Journal of Materials Chemistry* **2006**, *16*, 626–636.
8 F. X. Coudert, A. H. Fuchs, *Coordination Chemistry Reviews* **2015**, *307*, 211–236.
9 R. I. Walton, F. Millange in *The Chemistry of Metal-Organic Frameworks: Synthesis, Characterization, and Applications*, S. Kaskel (Ed.), Wiley-VCH, **2015**, chapter 24, pp. 729–764.
10 M. J. Van Vleet, T. Weng, X. Li, J. R. Schmidt, *Chemical Reviews* **2018**, *118*, 3681–3721.
11 K. S. Park, Z. Ni, A. P. Cote, J. Y. Choi, R. Huang, F. J. Uribe-Romo, H. K. Chae, M. O'Keeffe, O. M. Yaghi, *Proceedings of the National Academy of Sciences* **2006**, *103*, 10186–10191.
12 J. Cravillon, S. Münzer, S. J. Lohmeier, A. Feldhoff, K. Huber, M. Wiebcke, *Chemistry of Materials* **2009**, *21*, 1410–1412.
13 S. R. Venna, M. A. Carreon, *Journal of the American Chemical Society* **2010**, *132*, 76–78.
14 J. Cravillon, R. Nayuk, S. Springer, A. Feldhoff, K. Huber, M. Wiebcke, *Chemistry of Materials* **2011**, *23*, 2130–2141.
15 J. Cravillon, C. A. Schröder, R. Nayuk, J. Gummel, K. Huber, M. Wiebcke, *Angewandte Chemie - International Edition* **2011**, *50*, 8067–8071.
16 I. H. Lim, W. Schrader, F. Schüth, *Chemistry of Materials* **2015**, *27*, 3088–3095.
17 P. Y. Moh, P. Cubillas, M. W. Anderson, M. P. Attfield, *Journal of the American Chemical Society* **2011**, *133*, 13304–13307.
18 J. P. Patterson, P. Abellan, M. S. Denny, Jr., C. Park, N. D. Browning, S. M. Cohen, J. E. Evans, N. C. Gianneschi, *Journal of the American Chemical Society* **2015**, *137*, 7322–7328.
19 M. W. Terban, D. Banerjee, S. Ghose, B. Medasani, A. Shukla, B. A. Legg, Y. Zhou, Z. Zhu, M. L. Sushko, J. De Yoreo, J. Liu, P. K. Thallapally, S. J. L. Billinge, *Nanoscale* **2018**, *10*, 4291–4300.
20 S. F. Hulbert, *Journal of the British Ceramic Society* **1969**, *6*, 11–20.
21 J. D. Hancock, J. H. Sharp, *Journal of the American Ceramic Society* **1972**, *55*, 74–77.
22 M. Avrami, *The Journal of Chemical Physics* **1939**, *7*, 1103–1112.
23 M. Avrami, *The Journal of Chemical Physics* **1940**, *8*, 212–224.
24 M. Avrami, *The Journal of Chemical Physics* **1941**, *9*, 177–184.
25 J. Cravillon, C. A. Schroder, H. Bux, A. Rothkirch, J. Caro, M. Wiebcke, *CrystEngComm* **2012**, *14*, 492–498.
26 A. Polyzoidis, M. Etter, M. Herrmann, S. Loebbecke, R. E. Dinnebier, *Inorganic Chemistry* **2017**, *56*, 5489–5492.
27 P. Y. Moh, M. Brenda, M. W. Anderson, M. P. Attfield, *CrystEngComm* **2013**, *15*, 9672.
28 S. R. Venna, J. B. Jasinski, M. A. Carreon, *Journal of the American Chemical Society* **2010**, *132*, 18030–18033.
29 K. M. Ø. Jensen, C. Tyrsted, M. Bremholm, B. B. Iversen, *ChemSusChem* **2014**, *7*, 1594–1611.
30 H. H.-M. Yeung, Y. Wu, S. Henke, A. K. Cheetham, D. O'Hare, R. I. Walton, *Angewandte Chemie - International Edition* **2016**, *55*, 2012–2016.
31 Y. Wu, M. I. Breeze, G. J. Clarkson, F. Millange, D. O'Hare, R. I. Walton, *Angewandte Chemie - International Edition* **2016**, *55*, 4992–4996.

32 Y. Wu, S. Henke, G. Kieslich, I. Schwedler, M. Yang, D. A. Fraser, D. O'Hare, *Angewandte Chemie - International Edition* **2016**, *55*, 14081–14084.
33 Y. Wu, M. I. Breeze, D. O. Hare, R. I. Walton, *Microporous and Mesoporous Materials* **2017**, *254*, 178–183.
34 M. Drakopoulos, T. Connolley, C. Reinhard, R. Atwood, O. Magdysyuk, N. Vo, M. Hart, L. Connor, B. Humphreys, G. Howell, S. Davies, T. Hill, G. Wilkin, U. Pedersen, A. Foster, N. De Maio, M. Basham, F. Yuan, K. Wanelik, *Journal of Synchrotron Radiation* **2015**, *22*, 828–838.
35 A. F. Gualtieri, *Physics and Chemistry of Minerals* **2001**, *28*, 719–728.
36 I. Persson, *Journal of Solution Chemistry* **2018**, *47*, 560–567.
37 T. C. Bruice, G. L. Schmir, *Journal of the American Chemical Society* **1958**, *80*, 148–156.
38 M. A. Watzky, R. G. Finke, *Journal of the American Chemical Society* **1997**, *119*, 10382–10400.
39 S. Hoops, R. Gauges, C. Lee, J. Pahle, N. Simus, M. Singhal, L. Xu, P. Mendes, U. Kummer, *Bioinformatics* **2006**, *22*, 3067–3074.
40 R. J. Sundberg, R. B. Martin, *Chemical Reviews* **1974**, *74*, 471–517.
41 E. Kimura, Y. Kurogi, M. Shionoya, M. Shiro, *Inorganic Chemistry* **1991**, *30*, 4524–4530.
42 H. P. Bennetto, E. F. Caldin, *Journal of The Chemical Society A* **1971**, 2198–2207.
43 P. M. Forster, N. Stock, A. K. Cheetham, *Angewandte Chemie - International Edition* **2005**, *44*, 7608–7611.

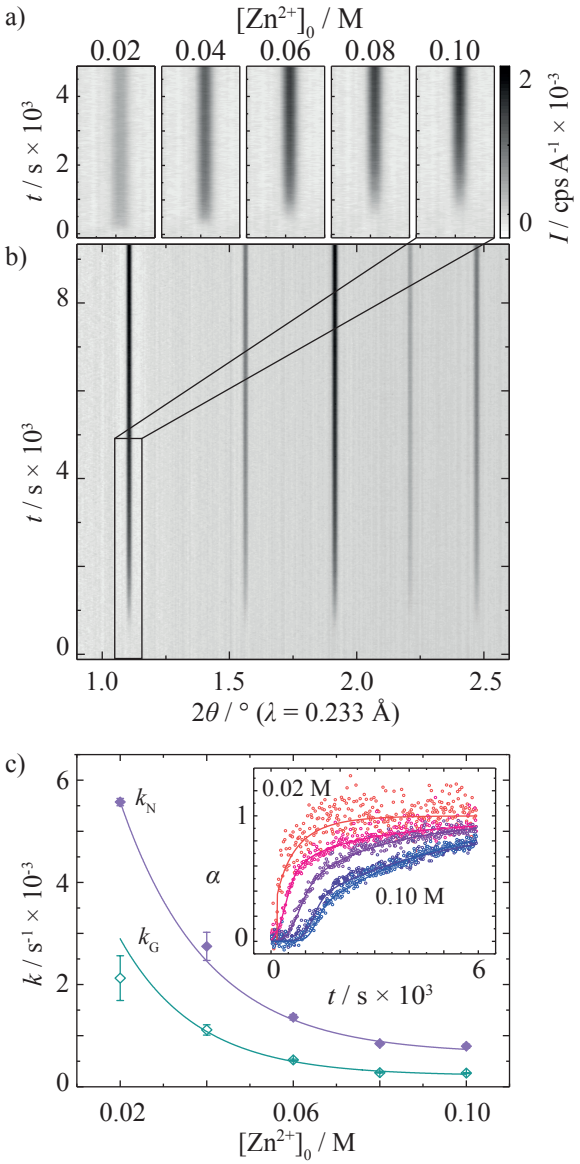

Fig. 1 *In situ* XRD of ZIF-8 formation, showing a) variation of the 110 peak as a function of time at different concentrations; b) an extended view for $[Zn^{2+}]_0$ = 0.10 M; and c) rate constants for crystal nucleation (k_N, purple closed diamonds) and growth (k_G, cyan open diamonds), calculated from Gualtieri fits to the changes in integrated XRD intensity, α, at five concentrations from $[Zn^{2+}]_0$ = 0.02 M to 0.10 M (inset).

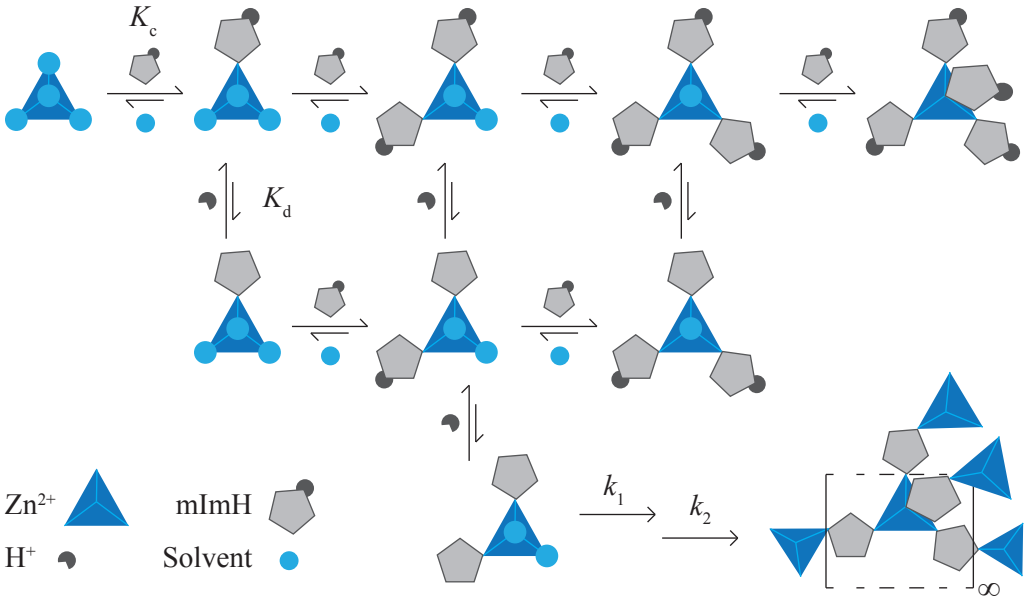

Fig. 2 Pre-equilibria in ZIF-8 crystallization resulting from coordination (right-to-left) and deprotonation (top-to-bottom), described by constants K_c and K_d, respectively, and self-nucleation and autocatalytic growth rates k_1 and k_2, respectively.

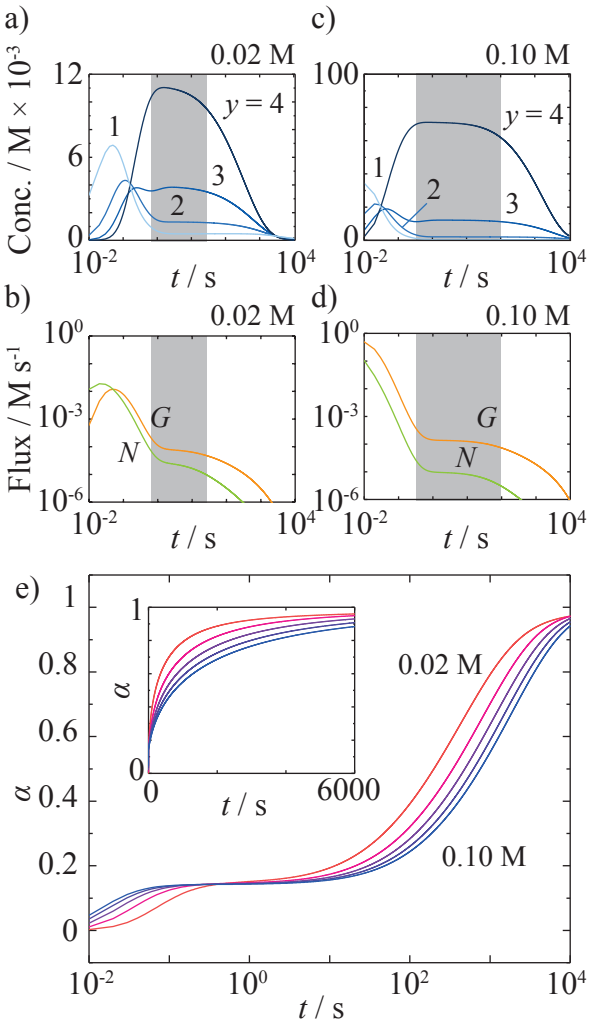

Fig. 3 Simulated evolution of pre-equilibrium intermediate monomer species with formula $[Zn(mImH)_y(S)_{4-y}]^{(2-x)+}$ (a, c) and flux of self-nucleation (labelled N) and autocatalytic growth (labelled G) reactions (b, d) for reactions with initial Zn concentrations of 0.02 M and 0.10 M. Regions shaded in grey mark periods during which pre-equilibrium is attained. Extent of crystallization, α, is shown as a function of time and concentration (e; inset shows the same data on a linear time axis c.f. Fig. 1c).

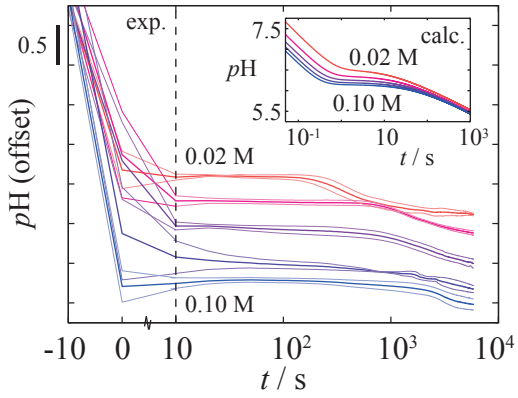

Fig. 4 Evolution of *p*H as a function of time and concentration, showing the rapid decrease that accompanies initial condensation events upon mixing, the pre-equilibrium plateau, and the second decrease that accompanies crystal growth. Curves are offset for clarity and bounded by standard deviations calculated from three independent measurements. Inset shows *p*H evolution calculated from the pre-equilibrium model.

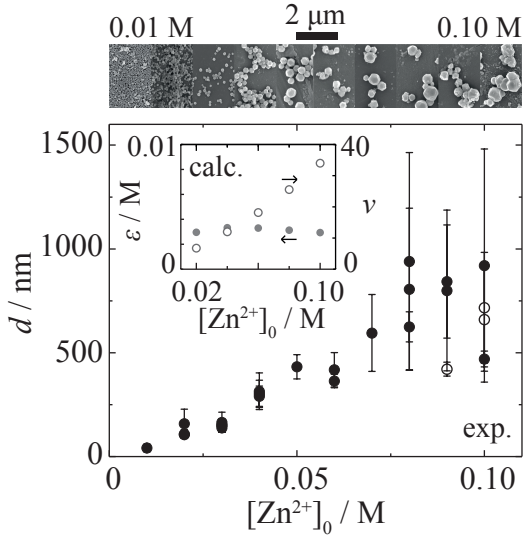

Fig. 5 Variation of particle diameter measured by SEM, d, with initial Zn^{2+} concentration, $[Zn^{2+}]_0$. Scale bar = 2 μm; open circles show statistics from images judged to be non-representative of the bulk sample. Inset shows nuclei concentration, ε (closed grey circles), and number of monomers per particle, ν (open grey circles), as a function of $[Zn^{2+}]_0$, calculated from the pre-equilibrium model.